# Self-assembly of chiral ligands on 2D semiconductor nanoplatelets for high circular dichroism

Henri Lehouelleur, Hong Po, Lina Makké, Ningyuan Fu, Leonardo Curti, Corentin Dabard, Céline Roux-Byl, Benoit Baptiste, Nathan van Zee, Thomas Pons, et al.

# Self-assembly of chiral ligands on 2D semiconductor nanoplatelets for high circular dichroism

*Henri Lehouelleur[1], Hong Po[1], Lina Makké[1], Ningyuan Fu[1], Leonardo Curti[1], Corentin Dabard[1], Céline Roux-Byl[1], Benoit Baptiste[2], Nathan J. Van Zee[3], Thomas Pons[1], Emmanuel Lhuillier[4], Jing Li[5,6], Sandrine Ithurria[1*]*

[1] Laboratoire de Physique et d'Etude des Matériaux, ESPCI-Paris, PSL Research University, Sorbonne Université UPMC Univ Paris 06, CNRS, 10 rue Vauquelin 75005 Paris, France

[2] Sorbonne Université, CNRS, Institut de minéralogie, de physique des matériaux et de cosmochimie, IMPMC, F-75005 Paris, France

[3] Chimie Moléculaire, Macromoléculaire, Matériaux, ESPCI Paris, Université PSL, CNRS, 75005 Paris, France

[4] Sorbonne Université, CNRS, Institut des NanoSciences de Paris, INSP, F-75005 Paris, France

[5] Université Grenoble Alpes, CEA, Leti, F-38000 Grenoble, France

[6]European Theoretical Spectroscopy Facility (ETSF), F-38000 Grenoble, France

* Corresponding author: sandrine.ithurria@espci.fr

**Abstract**

Group II-VI semiconductor nanoplatelets (NPLs) with atomically defined thicknesses and extended atomically flat (001) facets for ligand binding and chiro-optical effects. In this study, we demonstrate that tartrate ligands, anchored by two carboxylate groups, chelate the (001) facets of NPLs at an average ratio of one tartrate molecule to two cadmium (Cd) surface atoms. This assembly of chiral molecules on inorganic nanocrystals generates a circular dichroism g-factor as high as $1.3 \times 10^{-2}$ at the 1st excitonic transition wavelength of NPLs. Tartrate ligands induce an orthorhombic distortion of the initially "cubic" crystal structure, classifying the NPLs within the 222 point group. Unlike spherical nanocrystals, where it is difficult to discern whether chiral ligands affect only the surface atoms or the entire crystal structure, our findings unequivocally show that the crystal structure of NPLs is modified due to their thinness and atomic-scale precise thickness. The in-plane lattice parameters experience compressive and tensile stresses, significantly splitting the heavy-hole and light-hole bands. Additionally, tartrate ligands adopt different conformations on the NPLs surface over time, resulting in dynamic changes in the circular dichroism signal, including an inversion of its sign.

**Introduction**

Thanks to their 2D geometry, group II-VI semiconductor nanoplatelets (NPLs) are a fantastic playground for scientists.[1] By varying their composition or thickness, their optical properties can be tuned from the visible to the infra-red range.[2] The primary interest in NPLs arises from their 1D confinement with atomically defined thickness, which induces narrow optical features in both absorption and emission for homo- or hetero-structures. Additionally, due to their 2D shape, the NPLs display polarized optical properties which also vary with their lateral extension.[3,4] Recently, efforts have focused on introducing a further degree of anisotropy, such as chirality in the synthesis of circularly polarized emitters,[5] which may have applications[6] in telecommunication, biosensing[7,8] or display domains.[9,10]

The chiro-optical activity of nanocrystals can be achieved through several mechanisms, including (*i*) the synthesis of chiral shaped nanocrystals,[11,12] arising from defects or chiral reconstructions, (*ii*) the self-assembly of nanocrystals in chiral superstructures[13], (*iii*) Linear Dichroism-Lineal Birefringence (LDLB) phenomena or (*iv*) the surface binding of chiral ligands.[14] The "degree of chirality" is quantified by the dissymmetry factor, g, defined as $\Delta\varepsilon/\varepsilon$ where $\Delta\varepsilon$ represents the difference of extinction coefficient for left and right circularly polarized light, and $\varepsilon$ the total extinction coefficient. The g-factor is derived from measured circular dichroism ($CD_{meas}$) which is the sum of the intrinsic chiroptic circular dichroism $CD_{chiroptic}$, the LDLB interaction term $CD_{LDLB}$ and an artefact term $CD_{artefact}$ caused by the measurement set-up, which can usually be neglected with commercial instruments.[15]

Chiral shaped nanocrystals with *a priori* achiral crystal structure can be achieved by introducing a chiral entity into the reaction medium during particle growth.[14] This has been demonstrated with CdTe helices[13,16] and plasmonic gammadions[17]. Semiconductor NPLs are promising candidates for achieving similar conformations.[18,19] Indeed, NPLs have a thickness defined at the atomic scale such that the wide atomically flat top and bottom facets extend over thousands of $nm^2$.[1,20] They crystallize in either the wurtzite or the zinc blende (ZB) crystal structure, where their electroneutrality is ensured by surface ligands.[21–23] In ZB NPLs, the thickness aligns with the [001] direction, and two cationic planes terminate the surfaces with the total electroneutrality achieved through approximatively one carboxylate ligand per surface cadmium ($Cd_{surf}$). Besides, ZB CdSe NPLs present a four-fold inversion axis along the thickness. The top (001) and bottom $(00\bar{1})$ wide facets, while chemically equivalent, are rotated at 90° relative to each other. Thus, carboxylate ligands bind the $Cd_{surf}$ inducing tensile stress in perpendicular directions on the top and bottom facets.[20,24] Overall, NPLs can be seen as flexible substrates for the self-assembly of molecules which stress modifies their crystal structure.[25] The elastic energy is released by the folding of the particles either as twists, helices or scrolls depending on the lateral dimensions and orientation.[24,26,27] Consequently, individual folded NPLs capped with achiral carboxylate ligands are chiral objects. Theoretically, individual folded NPLs should display circularly polarized optical properties.[18,28,29] However, in practice, ensemble of these NPLs do not show any chiro-optical signal, considering that a racemic mixture of left and right handed shapes is obtained (see Figure S1).[30]

The second strategy involves the assembly of achiral nanoparticles into chiral superstructures.[13,31,32] Recently, wurtzite NPLs capped with chiral amine ligands were found to self-assemble in helical superstructures with g-factor on the order of $2\times10^{-2}$, despite exhibiting low individual g-factor[33]

In the third strategy, the CD signal does not originate from intrinsic chiro-optical property but rather from interferences between linear dichroism and linear birefringence in hierarchically structured materials. This CD signal is typically observed in nanocrystal films and is negligible in colloidal suspensions of nanocrystals.[15,34,35]

The fourth strategy, introduced by Balaz and co-workers in 2013, involves post-synthesis chiral ligand exchange on achiral particles.[36,37] This approach has since been applied to various ligands from thiolate[14] to carboxylate[38–41] anchoring groups. In these hybrid structures, chiro-optical activity can results from several factors: (*i*) the induction of chiral crystal structure by chiral ligands, as seen in hybrid organic inorganic perovskites,[42] (*ii*) chiral distortion of surface atoms on inorganic nanoparticles,[43,44] (*iii*) formation of crystal dislocations,[45,46] (*iv*) electronic interactions between the chiral molecule and the inorganic semiconductors[47] or (*v*) hybridization of the highest occupied molecular orbitals of the organic ligands and the valence band (VB) hole levels of nanocrystals.[48]

Among the various CdSe nanocrystal morphologies, more asymmetrical particles, tend to exhibit enhanced chiro-optical properties, as observed with nanorods and wurtzite NPLs.[49,50] ZB CdSe NPLs also display anisotropic g-factor in the order of $10^{-3}$ when capped with cysteine ligands.[41,50–52] Recently, Curti et al. proposed the design of a ligand derived from tartaric acid where one carboxylate function is replaced by an ester with an aliphatic chain. They achieve a dissymmetry g-factor of approximatively $2x10^{-3}$ for ZB CdSe NPLs at the 2$^{nd}$ exciton wavelength.[40] For ZB NPLs, chiral carboxylate ligands are particularly appealing since pristine NPLs present carboxylate ligands on their surface (a mixture of acetate and oleate). Notably NPLs, exhibit maximum CD signal at excitonic transition wavelengths, which contrasts with spherical particles whose CD signal are usually null at these transitions.[48]

In the frame of chiral nanoparticles with interactions in the visible range, the dissymmetry factor in absorption reaches values as high as $2.62 \times 10^{-2}$ for helically distorted 2D lead halide perovskites,[8,53] $5 \times 10^{-2}$ for nanographene, also called twistacenes or helicenes,[54,55] $2 \times 10^{-2}$ for Au 3D assemblies[56] or $5x10^{-2}$ for CdS MSCs films.[34]

In this study, we demonstrate the ligand exchange on CdSe NPLs from pristine carboxylates to chiral tartrates (TA), which feature two carboxylate terminations. This exchange occurs over several hours in ethanol and is facilitated by the presence of tri-octylphosphine (TOP). Both carboxylate terminations bind to the {001} facets of NPLs in a tilted geometry, leading to a pronounced orthorhombic distortion of the cubic crystal structure. One of the two in-plane lattice parameters expands by 3.3% while the other contracts by 3.3%. We show that the g-factor increases with the lateral extension of NPLs, ranging from $2 \times 10^{-3}$ to over $1.2 \times 10^{-2}$ at the wavelength of the first exciton transition, representing the highest values reported for similar systems.[57] We unequivocally demonstrate that NPLs are excellent flexible substrates for the assembly of chiral molecules, distorting the crystal structure along a point group 222 belonging to the 65 Sohncke-type space groups capable of forming chiral structures.[58] Additionally, the sign of the circular dichroism (CD) signal evolves over time without noticeable changes in absorption. These observations are attributed to a reconfiguration of ligands on the surface. DFT calculations indicate that tartrate ligands can bind to a (001) facet in two distinct conformations, with opposite footprints and comparable stabilization energies. We extend this ligand exchange to NPLs of varying thicknesses and compositions, including core/crown heterostructures.

**Results and discussion**

The ligand exchange from a mixture of acetate and oleate to TA has been optimized on 4 monolayer (ML) CdSe NPLs. These NPLs consist of 4 anionic planes alternating with 5 cationic planes with various lateral extensions. The exchange was conducted using only the levorotatory enantiomer of tartaric acid (L-TA) at room temperature in ethanol. The NPLs are suspended in ethanol, and a solution of TA in ethanol is further added along with TOP. The ligand exchange is monitored using absorption and circular dichroism spectroscopy. Although ethanol is a poor solvent for the NPLs capped with pristine acetate/oleate ligands, the stability of NPLs is improved as the ligand exchange progresses.

The ligand exchange from pristine carboxylate to tartrate ligands is sensitive to several factors including: (*i*) the molar ratio between tartaric acid and phosphine, (*ii*) the amount of tartaric acid introduced relative to $Cd_{surf}$ (see methods for the determination of $Cd_{surf}$ number) and (*iii*) the former surface chemistry and more precisely the ratio of long (oleate) and short (acetate) -chain ligands.

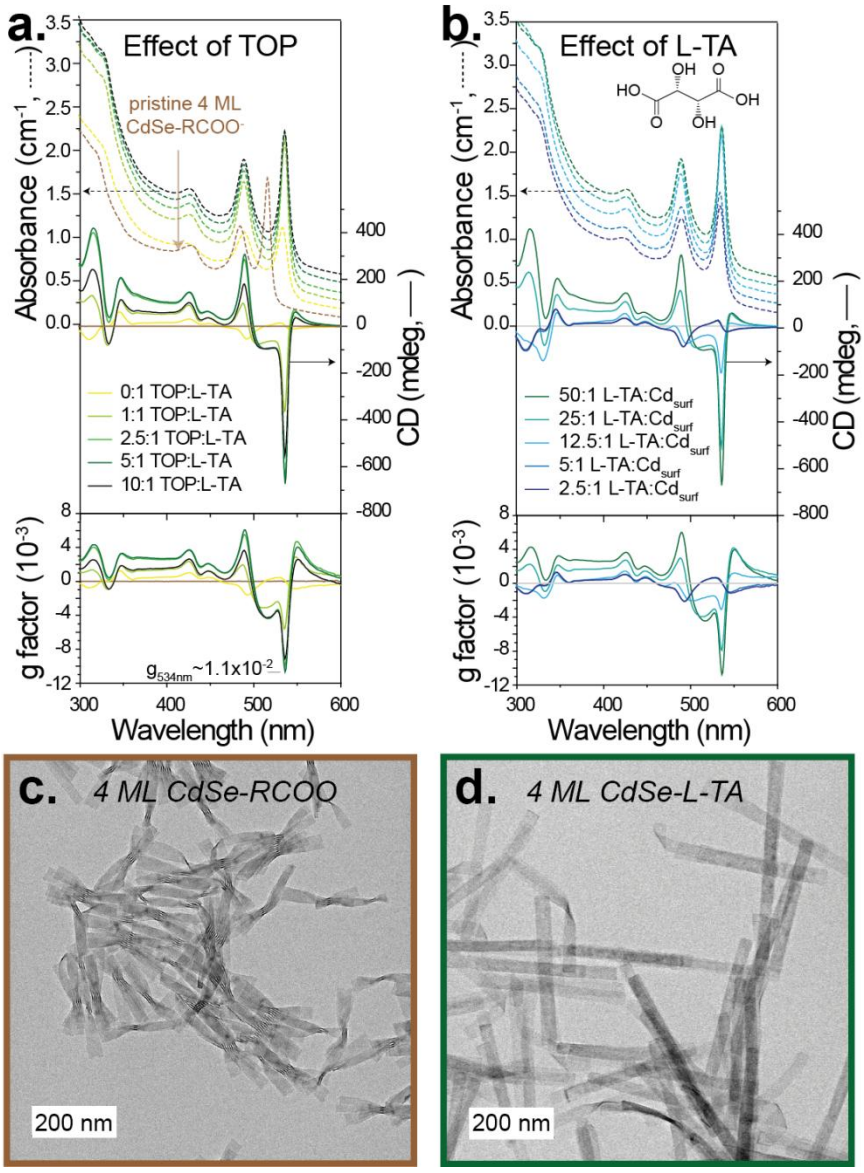

***Figure 1 :*** *-top- Absorption (straight lines), circular dichroism (dash lines) spectra, and –bottom- g-factor of 4 ML CdSe NPLs capped with L-TA obtained after 44 hours of exchange reaction (a.) with various amount of TOP, the TOP:L-TA molar ratio varies from 0:1 to 10:1 (keeping a constant molar ratio L-TA:$Cd_{surf}$ of 50:1) and (b.) various amount of L-TA, the L-TA:$Cd_{surf}$ molar ratio varies from 2.5:1 to 50:1 (keeping a constant molar ratio TOP:L-TA of 5:1). For clarity, the absorption spectra have been shifted by 0.1 OD. TEM images of 4 ML CdSe NPLs capped (c.) with Acetate/oleate and (d.) with L-TA after ligand exchange.*

In Figure 1a and b, we show the absorption and circular dichroism spectra of 4 ML CdSe NPLs exchanged with L-tartaric acid (L-TA) after 44 hours of exchange with increasing amounts of TOP and L-TA ligands compared to the $Cd_{surf}$ (Figure S1 to S3). The pristine carboxylate capped 4 ML CdSe NPLs exhibit two main transitions in absorption corresponding to the transitions of an electron from the heavy hole band to the conduction band and from the light hole band to the conduction band. They are respectively located at 513 nm (2.410 eV) and 484 nm (2.564 eV), the third one corresponds to the split-off transition.[21] After the ligand exchange, the two main transitions are shifted to 535 nm (2.319 eV) and 488 nm (2.543 eV). Such a shift of the optical features as a result of modified surface chemistry of NPLs is commonly attributed to a change in the thickness direction.[25] Indeed, NPLs' optical properties can be affected by ligands because of partial delocalization of the exciton over them and the band gap modification due to the in-plane stress. This red-shift reflects the ligand exchange and is in agreement with the literature.[40] Moreover, the spectral narrowness of the optical properties is preserved after ligand exchange, which is not the case for cysteine capped NPLs, for example.[50,51]

In Figure 1a, the L-TA to $Cd_{surf}$ molar ratio is kept constant and equal to 50, whereas the molar ratio TOP:L-TA is increased from 0:1 to 10:1. In absorption, all the spectra look similar, with the first excitonic peak at 535 nm, red-shifted compared to pristine 4 ML CdSe NPLs located at 512 nm. However, the intensity of absorption is lower with pure L-TA ligands in absence than in presence of TOP. Indeed, without TOP, the NPLs tend to dissolve after a few days in dilute concentrations while they remain stable in the presence of TOP, without any significant decrease in absorption over 10 days (Figure S4). Moreover, in the absence of TOP, in Figure 1a, the CD spectra present opposite trends compared to other spectra in the presence of TOP (opposite sign of the peaks corresponding to the $1^{st}$ and $2^{nd}$ exciton). It might be due to an incomplete ligand exchange or a partial change of ligand conformation as it will be discusses in the next section. Finally, the g-factor, which is independent of the concentration of NPLs after ligand exchange (Figure S5), shows the highest values for TOP:L-TA ratio from 2.5 to 10. This value reaches $1.1x10^{-2}$ at 534 nm which corresponds to the first exciton wavelength one of the highest values reported for nanocrystals capped with chiral ligands. This high g-factor corresponds to the first excitonic transition while being in the order of $5x10^{-3}$ for the second excitonic transition at 489 nm.

Moreover, it is essential to introduce enough TA ligands to replace the initial ligands and to ensure their adsorption on the NPLs surface. In Figure 1b, again all absorption spectra look similar, with a first excitonic transition at the same wavelength for various L-TA:$Cd_{surf}$ molar ratio. Nevertheless, with an insufficient amount of L-TA, the spectral peaks are slightly broadened and the CD spectra also show opposite trends to the case where the L-TA:$Cd_{surf}$ molar ratio is superior to 10. It most probably comes from an incomplete ligand exchange. The nature of the outgoing ligand also modifies the ligand exchange efficiency. With an acetate rich surface, the ligands exchange is faster compared to an oleate rich surface (Figure S6). This may be explained by the steric hindrance

brought by the ligand tails which hinders the arrival of incoming molecules. Thus, the time for a full ligand exchange can vary from one experiment to another, from few hours to 2 days.

The presence of the phosphine is beneficial for the ligand exchange. After ligand exchange, when NPLs are precipitated, the presence of phosphorus is not detectable by EDX (Table S1), showing its low affinity for the NPLs' surface. Indeed, hydrogen bonds between the hydroxyl group of the tartaric acid and the phosphine are very unlikely since the electronegativity of the phosphorous is too low. Replacing the trioctylphosphine by tributylphosphine lead to equivalent results, but amines (oleylamine or trioctylamine) tend to dissolve NPLs or lead to incomplete ligand exchange (Figure S7). In the following, we will keep the L-TA:$Cd_{surf}$ and TOP:L-TA molar ratio respectively of 50:1 and 5:1. In these conditions, TEM images show that the 2D shape is preserved after ligand exchange (Figure 1d). Besides, we observe an unfolding of NPLs after ligand exchange (Figure 1c) which may be explained by a relaxation of the stress brought by incoming ligands.

In order to understand the effect of chiral ligands on the optical properties of NPLs, the kinetics of a ligand exchange have been followed by circular dichroism spectroscopy at room temperature. Figure 2a and b show the absorption and CD spectra of acetate-enriched 4 ML CdSe NPLs during the ligand exchange from 1 minute to 240 minutes. The ligand exchange happens in two phases, the first one at short time range lasts around 20 minutes (Figure 2a) while the second one, at long time range, lasts for several hours (Figure 2b).

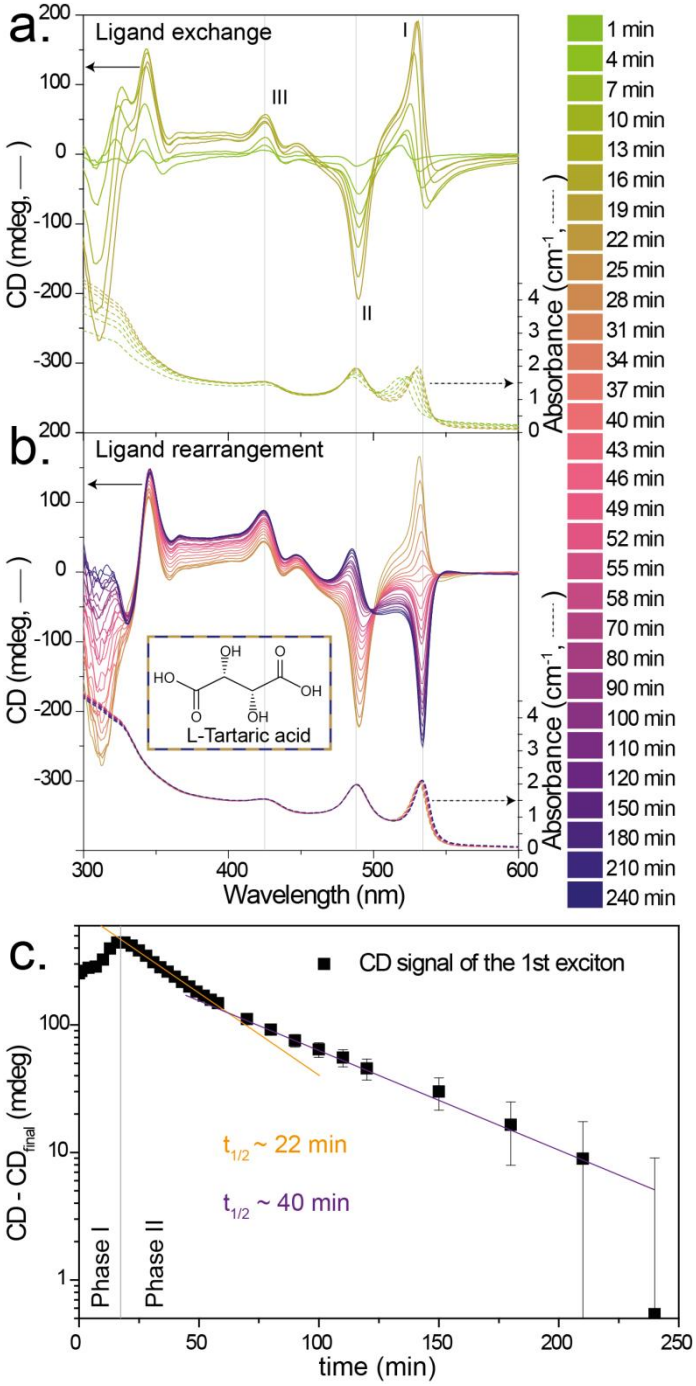


***Figure 2 :*** *Absorption (dash lines) and circular dichroism (straight lines) spectra during a ligand exchange from pristine carboxylate to L-tartaric acid (a.) from 1 minute to 19 minutes and (b.) from 22 minutes to 240 minutes. (c.) Plot of the evolution of the CD signal corresponding to the 1st excitonic transition as a function of time. The difference between the CD signal and the final CD signal has been plotted.*

During the first 20 minutes, the absorption spectra undergo a red-shift, accompanied by the emergence of CD signal (see Figure 2a). This CD signal is attributed to the transfer of chirality from the chiral ligands to the nanocrystals. The two primary CD signals (denoted I and II) correspond to the first two excitonic transitions: the first one (I) at lower energy is positive while the second transition (II) at higher energy is negative. In the second phase of ligand exchange, occurring between 20 and 240 minutes, the absorption spectra show minimal variation (see Figure 2b) suggesting that changes in surface chemistry are limited. The stress induced by the ligands and the dielectric environment

remain relatively constant. However, the CD spectra evolve significantly during this phase. The CD signal from the first excitonic transition changes from a positive contribution to a negative contribution while the CD signal from the second transition changes from negative to positive. Such a change in the sign of the nanocrystal CD signal are uncommon, though similar behavior has been reported in metal complexes and attributed to changes in the conformation of the complexing molecule.[59] Figure 2c represents the difference between the CD signal values at various time and the final CD signal plotted on a logarithmic scale. In the second phase, the linear trend with two different slopes suggests a first-order kinetic reaction, with a transformation of species A into A'. From this analysis, we determine two half-lives: 22 min for the first phase (orange in Figure 2c) and 40 min for the second phase (purple in Figure 2c). The kinetic rate of these two phases can be accelerated with increasing temperature without modifying the various stages of the exchange (Figures S8 and S9). L-TA ligands on the surface of NPLs may undergo a conformational change over time. Consequently, it is crucial to understand how the ligands bind to the NPLs surface. The two phases identified correspond to an initial ligand exchange, followed by a secondary process that substantially alters the chiro-optical activity of NPLs.

To probe the anchoring behavior of the tartrate ligands, aliquots have been taken throughout the ligand exchange process and analyzed by absorption, emission and FTIR spectroscopy (Figure 3b). Reasonably, the red-shift concerns both the absorption and the emission (Figure 3a). However, this shift may be intriguing, given that both outgoing and incoming ligands possess carboxylate anchoring groups. It suggests different coordination modes of the carboxylate ligands. In emission (Figure 3 dash lines), a broad deep trap emission appears in the first 120 minutes, likely due to poor surface passivation. After 120 min, only band edge emission is detected, indicating improved passivation of surface dangling bonds by L-TA ligands.

Carboxylate anchoring groups exhibit different binding modes, which can be identified by the splitting Δν between the symmetric and antisymmetric stretching modes of the COO function in the 1350 to 1650 $cm^{-1}$ range.[60–63] For a monodentate carboxylate, where only one oxygen binds to a metal atom, Δν is > 200 $cm^{-1}$. In a bidentate chelating mode, where both oxygens bind to the same metal atom, Δν is typically around 100 $cm^{-1}$. For a bidentate bridging mode, where the two oxygens bind to two different metal atoms, Δν > 140 $cm^{-1}$. Finally, in the tilted-bridge geometry, one oxygen bridges two metal atoms while the other binds to one metal with a splitting similar to that of the bidentate geometry.

The FTIR spectra of pristine NPLs exhibit characteristic $CH_2$ bond vibrations around 2800 $cm^{-1}$ and the antisymmetric and symmetric stretching modes of the COO at 1534 $cm^{-1}$ and 1439 $cm^{-1}$. Here, the splitting Δν of 95 $cm^{-1}$, confirms a chelating geometry for the carboxylate ligands (Figure 3b).[60] By this way, the surface Cd are on average in a tetrahedral environment. A minor vibration at 1408 $cm^{-1}$ is attributed to acetate ligands bound in a tilted geometry on the surface. Then, during ligand exchange a new vibration emerges at 1581 $cm^{-1}$, eventually replacing the signal at 1534 $cm^{-1}$ which completely disappears. The primary symmetric vibration of the COO function is observed at 1404 $cm^{-1}$ yielding a Δν of 177 $cm^{-1}$, indicating a carboxylate ligand in a tilted geometry. Additionally vibrations around 1075 $cm^{-1}$ are attributed to the C-O stretching from the alcohol while the broad band between 3100 $cm^{-1}$ and 3600 $cm^{-1}$ corresponds to the O-H bonds with hydrogen bonds. In Figure 3c, we plot the percentage contribution of COO antisymmetric stretching vibrations from carboxylates in chelating (and tilted geometries) and the positions of the first excitonic positions

along the ligand exchange. When the first excitonic peak reaches saturation at 535 nm (2.32 eV), no chelating carboxylate ligands remain on the surface, suggesting a complete transition to tilted geometry.

The TA molecule, with its two carboxylic functions, exhibits strong chelating behavior. On the NPL surface, it seems that both carboxylate groups bind to the surface, as only one antisymmetric COO vibration is observed at the end of the exchange. For comparison, NPLs exchanged with terephthalic acid (Benzene-1,4-dicarboxylic acid) exhibit two distinctive COO antisymmetric stretching modes in FTIR specta corresponding to one carboxylate bound to the surface and the other remaining as a free carboxylic acid (Figure S8). Therefore, we conclude that both carboxylic terminations of the TA bind to the NPLs surface in their deprotonated form to ensure the NPLs neutrality. On average, one tartrate ligand coordinates to every two $Cd_{surf}$ (Figure 3d).

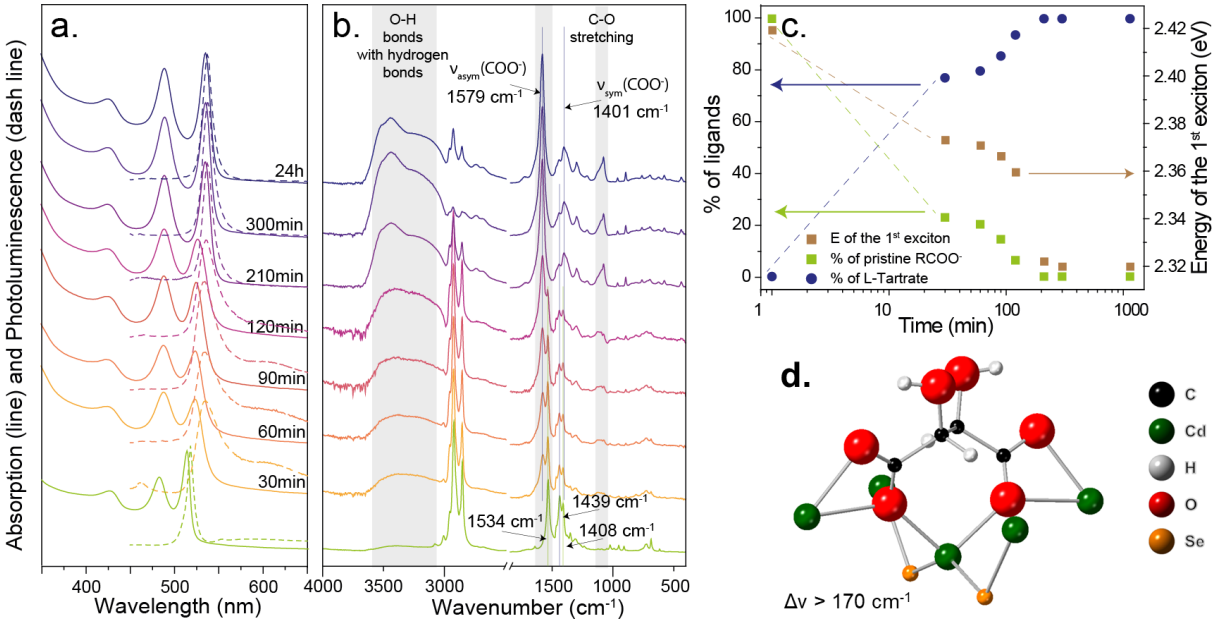


***Figure 3 :*** *(a.) Absorption (straight lines) and emission (dash lines) of 4 ML CdSe NPLs during a ligand exchange from pristine carboxylate to L-TA (b.) FTIR spectra of the corresponding aliquots (c.) Percentage of carboxylate and L-TA ligands where the sum of the two is equal to 100%, and energy of the first exciton over time during the ligand exchange. (d.) L-TA ligand on a (001) facet showing the tilting geometry of the two carboxylate functions.*

An additional point worth noting is that before and after circular dichroism signal inversion, the infrared spectra are similar, pleading again for a weak modification of the NPLs environment during this inversion (Figure S11).

To investigate the anchoring tendency and conformations of tartrate ligands on NPLs, density functional theory (DFT) calculations were performed on 4 ML CdSe NPLs capped with L-TA ligands. The initial step involved determining the ligands organization either aligned with the [100] direction (referred to as configuration 1 in Figure 4) or along the [110] direction on the (001) facet of the ZB crystal structure (referred to as configuration 1', Figure S12). The stabilization energy per unit cell (2a × 2b) is lower for configuration 1 compared to configuration 1', leading us to focus on configuration 1, where there is one TA molecule per ZB surface cell (Table S2). Figure 4a illustrates the L-TA adsorbed on the surface of the NPLs in configuration 1. Examining the relaxed NPLs at the edge

(Figure 4b), the carbon-hydroxyl bonds of the TA are oriented perpendicular to the (001) facet of NPLs. The carboxylate functions are adsorbed on the surface in a tilted geometry, consistent with the results from FTIR spectroscopy. One of the oxygen bridges two cadmiums while the second oxygen binds to a single cadmium atom. In this geometry, half of the $Cd_{surf}$ atoms are in an octahedral environment, coordinated by two selenium and four oxygen atoms, while the other half are in a tetrahedral environment, coordinated by two selenium and two oxygen atoms. Figure 4c and d illustrate the top and bottom facets along the [001] direction. It can be observed that the backbone of the L-TA ligand forms an "S"-shaped pattern on the surface. After cell relaxation, the in-plane lattice parameters a and b become unequal, and both differ from the lattice parameter c in the thickness (Table S2). Therefore, the crystal structure is neither cubic nor tetragonal, but orthorhombic with a 222 point group symmetry. This configuration in which the hydroxyl groups are oriented perpendicular to the NPL surface, appears to be the most stable, thanks to intramolecular hydrogen bonding and minimal steric hindrance (dotted lines on Figure 4b,c,d).

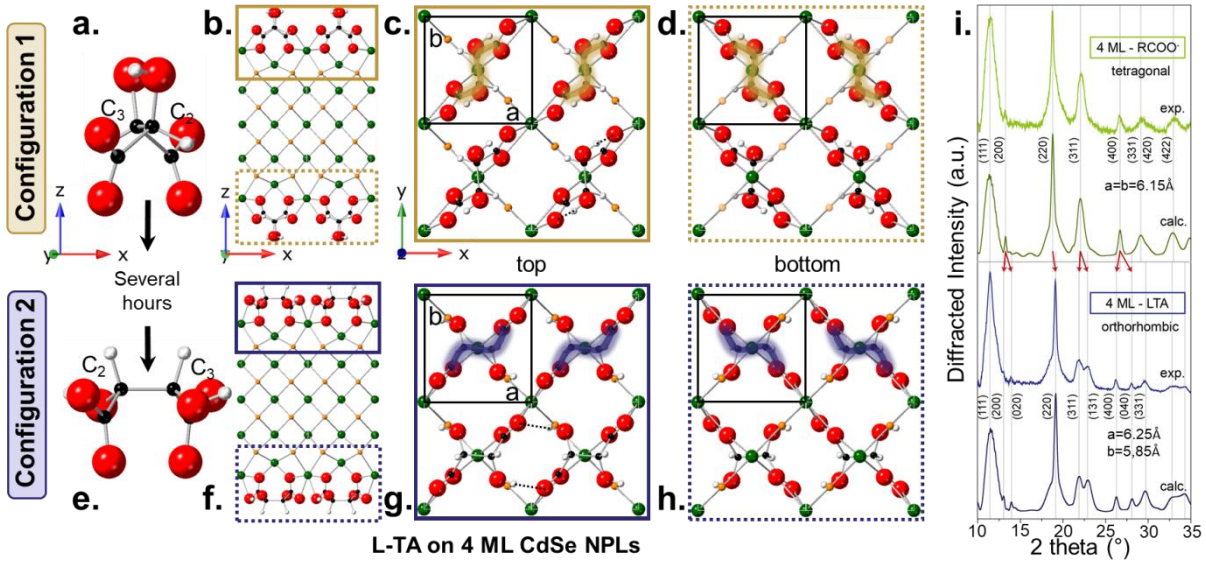


***Figure 4 :*** *Possible binding of L-TA ligands on 4 ML CdSe NPLs. Configuration 1 (a.) In this conformer of L-TA the COH bonds are "perpendicular" to the NPLs (x-y) plane. (b.) projection of the NPLs in the [010] direction. Projection of (c.) the top and (d.) the bottom facets of a NPL capped with L-TA in the [001] direction. The beige curve line represents the skeleton of the L-TA in configuration 1 with an S shape. Configuration 2 (e.) In this conformer of L-TA the COH bonds are "parallel" to the NPLs (x-y) plane. (f.) projection of the NPLs in the [010] direction. Projection of (g.) the top and (h.) the bottom facets of a NPL capped with L-TA in the [001] direction. The blue curved line represents the skeleton of the L-TA in configuration 2 with a Z shape. (i.) Experimental and calculated X-Ray diffraction patterns of 4 ML CdSe NPLs before (in green) and after (in blue) ligand exchange from $RCOO^-$ to L-TA ligands. The source is Mo Kα radiation.*

However, an alternative configuration (configuration 2 in Figure 4), which differs from configuration 1 by the position of the hydroxyl groups, and which presents a slightly higher stabilization energy per unit cell compared to configuration 1 (-228.87 eV/unit cell for configuration 1 and -229.30 eV/unit cell for configuration 2, Figure S13 and Table S3). In configuration 2, the carbon-hydroxyl bonds are oriented parallel to the (001) facet of NPLs (Figure 4e). This reorientation of the hydroxyl groups causes a nearly 90° rotation of the $C_2C_3$ bond relative to configuration 1. Consequently, the footprint of the L-TA on the NPLs facet forms a "Z" shape (Figure 4g). It is thus inverted compared to configuration 1, but again the COO binds the surface in a tilted orientation and

the point group symmetry remains 222. In configuration 2, there are intermolecular hydrogen bonds and after cell relaxation the lattice gets also distorted in orthorhombic structure (Figure S13 and Table S3).

Chemically, these two configurations are similar, featuring identical binding geometries and density of ligands. However, their asymmetric footprints on the NPLs surface are opposite, leading us to hypothesize that the observed change in CD signal sign over time, observed in Figure 2, is due to a transition between these two configurations. Configuration 1, with hydroxyl groups oriented outward from the NPLs, might represent the initial configuration due to minimal steric hindrance. Experimentally, it has been shown that the heavy-hole exciton transition dipoles of NPLs coincide with the NPL plane, while the light-hole and split-off excitons present a finite dipole projection along the z direction which coincides with the thickness of NPLs.[64] Thus, as the ligands imprint a chiral footprint on the NPL surface (x-y plane), an inversion in this footprint (from "S" to "Z") should change the chirality, thus inducing a reversal of CD signal for the first two transitions. To conclude, the process appears to involve an initial step where acetate/oleate ligands are exchanged for tartrate, accompanied by a shift in absorption, followed by a second step involving a change in tartrate configurations and a corresponding inversion of the CD signal. The duration of this second step is highly dependent on the exchange temperature and may be a thermodynamic stabilization (Figures S8 and S9). Besides, we have noticed that depending on the nature of the native carboxylate ligands, these two steps can occur simultaneously with the inversion of the CD signal along with the absorption shift.

As simulated by DFT calculation, the TA ligands distort the cubic crystal structure of NPLs, a distortion that is further confirmed by X-ray diffraction (Figure 4i). Figure 4i presents the XRD patterns of 4 ML CdSe NPLs before (top of Figure 4i) and after full ligand exchange (bottom of Figure 4i) from acetate/oleate to tartrate ligands. The NPLs are suspended in a capillary to prevent preferential orientation of NPLs on a substrate, with Mo Kα radiation serving as the source. When interpreting the XRD patterns of NPLs, three key factors must be considered: the NPLs dimension e x W x L (where the thickness e is much smaller than the width W and the length L of the NPLs), the crystal distortion due to ligand interactions and the possible transition from flat to helical structures. It is well established that native carboxylate ligands induce a tetragonal distortion, as evidenced by the shifted peaks in the XRD pattern compared to the ideal cubic structure.[20,25,30] The main prominent peaks correspond to the (111), (220), (311) and (400) planes of the distorted "cubic" crystal structure. The (220) peak reflects the structural distortion, as the NPLs thickness aligns along the [001] direction, the (220) is not equivalent and is split compared to the (202) and (022) planes. The (220) Bragg peak is narrow due to the large lateral dimensions of NPLs (in zone with the [001] direction, the thickness of NPLs) and is associated with the in-plane distortion. Its shift to smaller angles for carboxylate capped NPLs indicates the tetragonal distortion and the tensile in-plane stress. The other two contributions (202) and (022) are broad. The presence of the $\bar{4}$ axis and in-plane stress induce the folding of NPLs into helical structures.[30] Consequently, the (220) peak further splits into a narrow contribution from planes normal to the helix axis, which helps determine the in-plane lattice parameter, and broad contributions, which splitting depends on the helix radius.[30] The distortion is also evident in the (400) peak, which shows contributions from both the (400) and (040) planes, while the (004) contribution is negligible NPLs limited thickness. The calculated XRD pattern for a tetragonal cell with a=b=6.15 Å and c=6.05 Å shows excellent agreement with the experimental data (Figure 4i top).

After ligand exchange, NPLs unfold (Figure 1d) and the (220) peak shifts to larger angles, indicating a reduction in the interplanar spacing (Figure 4i bottom). Interestingly, the (311) and (400) peaks split on either side of the pristine NPLs peaks, one corresponding to a larger and the other to a smaller interplanar distance compared to pristine NPLs, which suggests an orthorhombic distortion of the crystal structure. From the XRD pattern, we deduce the in-plane lattice parameters a and b of 6.25 Å and 5.85 Å, while variations in c are negligible remaining approximately c = 6.05 Å (see Figure S12 for adjustments). The NPLs capped with L-TA ligands exhibit both compressive and tensile in-plane stresses of ±3.3%. These values, though particularly high, are consistent with observations for other types of ligands on NPLs that induce significant surface stress.[30] The origin of chirality in such systems is often debated—whether it arises from surface effects or distortions in the crystal structure. In the case of NPLs, it appears that chiral ligands induce a structural distortion following a 222 point group symmetry which belongs to the 65 Sohncke-type space groups capable of supporting chiral structures.[58] This structural flexibility is achieved by the 2D nature of NPLs.

Actually, this orthorhombic distortion strongly affects the NPLs optical properties and in particular the splitting between the two first excitonic transitions (Figure S13).[65] Ligand exchanges on ZB NPLs have been established from carboxylates to halide,[24] thiolate[25,66] or phosphonate ligands;[25] following the previous order the first excitonic peak shows an increasing red-shift.[67] This shift is explained by the in-plane surface stress brought by the ligands which is compensated by an out of plane stress of the opposite sign. For example, the in-plane tensile stress brought by native acetate/oleate ligands induces a compressive stress in the thickness, while the phosphonate and to a lower extent thiolate ligands bring an in-plane compressive stress and hence an out-of-plane tensile stress. These modifications of the thickness and the effective masses of the charges can lead to band bending and a red-shift of the optical properties.[65] With halide ligands, the stress is relaxed and the energy of the first excitonic transition lies between acetate/oleate and thiolate ligands.[24,25,67] With tartrate ligands, the first excitonic peak is at an intermediate energy between carboxylate and halide ligands pleading for an intermediate out-of-plane stress close to relaxation. This is consistent with TEM observation that NPLs appear less folded after the TA ligand exchange in comparison to the original oleate/acetate capped NPLs. In addition, with TA ligands, we observe an increase in the energy splitting between the first two excitonic transitions (difference of energy between the heavy hole and the light hole). This splitting gives an insight into the in-plane stress and diminishes as the in-plane stress is reduced.[67,68] With tartrate ligands, the splitting is the largest over all the other types of ligands studied on NPLs. It thus appears that, even though the out-of-plane stress is reduced, the in-plane stress is strong with both a tensile stress and a compressive stress in the [100] and [010] directions. With conventional ligands, the top and bottom facets are submitted to two stresses oriented at 90° from each other in the [110] and $[1\bar{1}0]$ directions, leading to an overall tetragonal distortion. With TA ligands that are chelating with their two carboxylate anchoring groups, the top and bottom facets are submitted to two stresses respectively oriented at 90°±β from each other in the [110]+β/2 directions and $[1\bar{1}0]$-β/2 directions leading to an overall orthorhombic distortion.

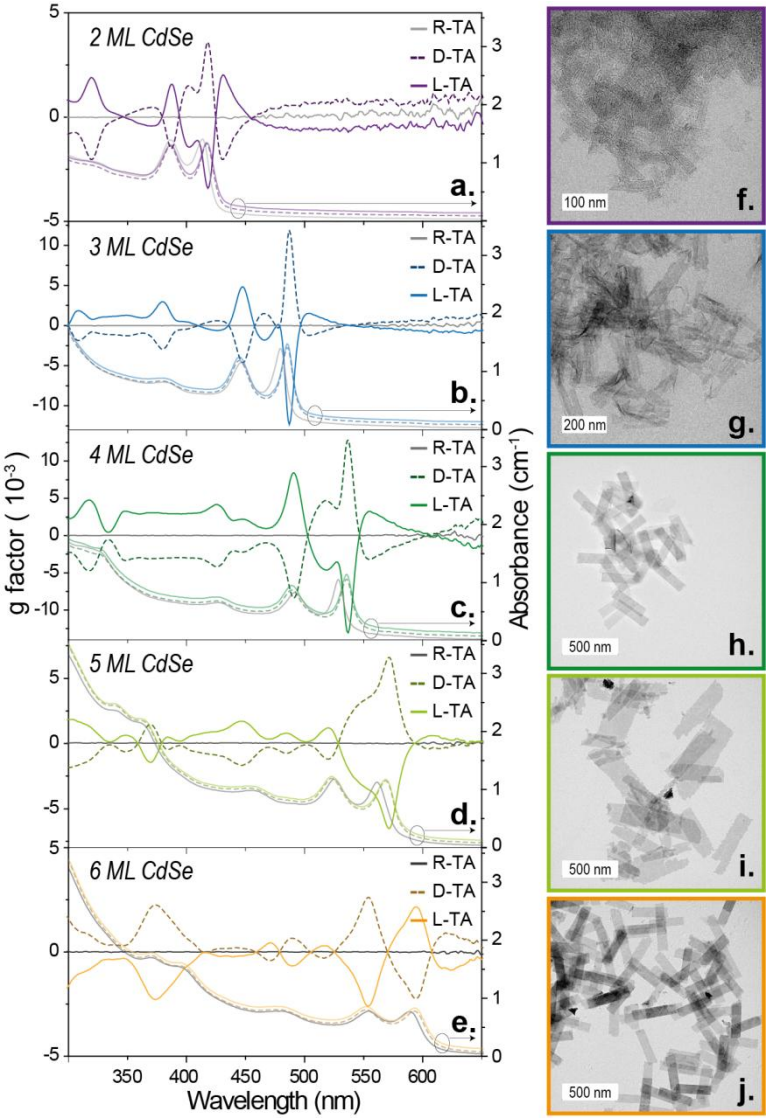


***Figure 5 :*** *Absorption and g factor spectra of (a.) 2 ML, (b.) 3 ML, (c.) 4ML, (d.) 5 ML and (e.) 6 ML CdSe NPLs capped with R-TA, L-TA and D-TA. TEM pictures of (f.) 2 ML, (g.) 3 ML, (h.) 4ML, (i.) 5 ML and (j.) 6 ML CdSe NPLs capped with L-TA ligands.*

Finally, the ligand exchange was applied to CdSe NPLs with various thicknesses (Figure 5) and to other compositions such as CdTe, CdSeTe and core/crown CdSe/CdS (Figure S14). Figure 5 presents the absorption spectra and asymmetric g-factor of NPLs capped with L-TA, D-TA acid and R-TA (a racemic mixture of L- and D-TA) (Figure S15). In all exchanges, a red-shift of the optical features is observed, with this shift being more pronounced for the pure enantiomers of TA compared to the racemic mixture. The energy splitting between the first two excitons is consistently larger for all populations compared to pristine and bromide capped NPLs (Figure S12). Furthermore, as expected, the g-factors curves for the two enantiomers are mirror images, while NPLs capped with the racemic mixture displays no CD properties. The g-factor corresponding to the first excitonic transition of 2 ML CdSe NPLs is approximately $3x10^{-3}$ at 418 nm, and for 3 ML and 4 ML CdSe NPLs, it exceeds $1.1x10^{-2}$ at 487 nm and 535 nm respectively. For these 3 and 4 ML NPLs which present high g-factor, linear dichroism measurements have been performed to confirm that the LDLB phenomenon was negligible, contributing less than 1% of the total CD signal (Figure S16 and Tables S5 and S6). For 5 ML CdSe NPLs, the g-factor peaks at 571 nm with a value of $6x10^{-3}$. For 6 ML NPLs, the g-factor

reaches 2.35 x $10^{-3}$ at 594 nm for the 1st exciton and 2.60 x $10^{-3}$ at 553 nm for the 2nd exciton. Notably, in contrast to other populations, is the 6 ML NPLs exhibit a reversed signal with a positive CD signal for the 1st excitonic transition for L-TA capped NPLs, without any inversion of the CD signal over time. This difference may be attributed to the 6 ML NPLs synthesis via colloidal Atomic Layer Deposition, which could introduce surface defects. These defects, likely hinder the full self-assembly of molecules reducing intermolecular hydrogen bonding and preventing efficient surface molecular rearrangement. Additionally, switching between configurations may induce cause surface reorganization, which becomes more challenging as NPLs thickness increases. Thick NPLs are also less flexible substrates.

Finally, the effect of lateral extension on the g-factor was studied. Similar trends were observed for both 3 ML and 4 ML CdSe NPLs, where the g-factor at the 1st excitonic transition increases with the lateral extension, reaching values up to $1.3 \times 10^{-2}$ for large lateral extensions, compared to $2 \times 10^{-3}$ for smaller lateral extensions. When plotting the g-factor of the two populations on the same graph, the data appears to follow a similar slope. However, further experiments are necessary to confirm this trend. (Figures S19 to S21).

**Conclusion**

In conclusion, we have demonstrated an efficient ligand exchange from native acetate/oleate to tartrate ligands, facilitated by the presence of TOP, on CdSe NPLs. This process can be extended to other cadmium chalcogenides NPLs. The use of these chiral ligands enables NPLs to exhibit a high CD dissymmetry factor, exceeding to 1x$10^{-2}$ at 1st excitonic transition wavelength. We attribute this significant value to a combined effect of the self-assembly of TA ligands on the extended {001} facets of NPLs and the orthorhombic distortion of the cubic crystal structure, an effect which should not be detectable with spherical particles. Specifically, the TA ligands act as chelating ligands on the {001} facets of NPLs via their two carboxylate groups. During ligand exchange, we observe an inversion in the sign of the CD signal, which may be attributed to a change in ligand conformations from one in which the hydroxyl groups are oriented perpendicular to the NPLs surface, to one where they are aligned parallel on the NPLs surface. This conformational change induces a tilting of the ligand footprint on the surface. From a synthetical point of view, incorporating these chiral ligands during the NPLs growth could be advantageous for inducing an enantioselective growth, potentially yielding NPLs all folding in the same direction.

**Experimental section**

Chemicals:

Octadecene (ODE) (Sigma-Aldrich, 90%), Cadmium acetate dihydrate ($Cd(Ac)_2.2H_2O$) (Sigma-Aldrich, 99.995%), Cadmium oxide (CdO) (Strem Chemicals, 99.99%), Myristic acid (Sigma-Aldrich, 99%), Selenium powder (Se) (Strem Chemicals, 99.99%), Oleic acid (OA) (Sigma-Aldrich, 90%), Sodium borohydride (NaBH4) (Sigma, 99%), Tri-octylphosphine (TOP) (Alfa Aesar, 90%), Tri-butylphosphine (TBP) (Cytec, Solvay), Oleylamine (OLAm) (Acros, 80–90%), Tri-octylamine (TOA) (Sigma-aldrich, 98%), L-(+)-tartaric acid (L-TA) (Sigma-Aldrich, 99%), D-(-)-tartaric acid (D-TA) (Sigma-Aldrich, 99%), DL-tartaric acid (R-TA) (Sigma-Aldrich, 99%), Terephtalic acid (Sigma-Aldrich, 98%), n-hexane (VWR, 99%), ethanol (VWR, 99%), methanol (MeOH) (VWR), N-methylformamide (NMF) (Alfa Aesar, 99%) were used as received.

**Preparation of Precursors**

Cadmium Myristate ($Cd(Myr)_2$) : In a three-neck flask, 2.56 g of CdO and 11 g of myristic acid are mixed and degassed at 70 °C for 30 min, after which the heating temperature is increased to 200 °C under argon flow until the solution turns colorless. The temperature is then decreased to 60°C and around 20 mL methanol is added. The final product is precipitated and washed with methanol before being left to dry under vacuum overnight.

Tri-octylphosphine Selenide Solution (TOP-Se, 1M): In a glovebox, 20 mL of tri-octylphosphine and 1.58 g of selenium powder are stirred overnight until a colorless solution is obtained. This final product is later stored in the glovebox to prevent it from oxidizing.

Se-ODE 0.1M : In a 25 mL three-neck flask are introduced 79 mg of Se powder with 10 mL ODE. After degassing for 10 min at room temperature, the atmosphere is switched to Ar and the heater is set to 200°C. At 200°C, the reaction is kept for 2 h. The final Se-ODE 0.1 M solution is kept in a glovebox to prevent degradation with air.

Synthesis of NPLs

*Synthesis of 2 ML CdSe NPLs :* In a three-neck flask, 160 µL of OA, 260 mg of $Cd(Ac)_2.2H_2O$ and 20 mL ODE were degassed at room temperature for 1 h. The atmosphere is then switched to Argon, and the temperature is set to 160°C. A growth solution made of 250 µL TOP-Se 1M and 500 µL ODE is injected at 120°C. The mixture is left at 160°C for 1h before being cooled down to room temperature. During the cooling process, 2 mL of OA is injected into the flask. The particles are washed before being redispersed in 10 mL hexane. The number of surface cadmium is estimated thank to the synthesis procedure of each particles, in the hypothesis that the selenium is the limiting product and that all Se precursor reacted. For 2MLs CdSe NPLs, the total amount of Se in NPLs is the initial amount of TOP-Se, that is 0.25 mmol. There are 2 planes of Se and 2 planes of Cd at the surface, which corresponds to 0.25 mmol. The particles are suspended in 10 mL, so the concentration of surface Cd is 0.025 mmol/mL.

*Synthesis of 3 ML CdSe NPLs :* In a three-neck flask, 240 mg $Cd(Ac)_2.2H_2O$ and 15 mL of ODE are degassed at 60°C for 30 min. Under Argon, the mixture is heated up to 190°C. A solution of 600 µL of TOP-Se 1M, 200 µL OA and 5 mL ODE is then added at a rate of 4 mL/h. After the complete injection of the growth solution, the heat is removed and the particles are then washed and suspended in 10 mL hexane. For 3ML CdSe NPLs, the total amount of Se in NPLs is the initial amount of TOP-Se, that is 0.6 mmol. There are 3 planes of Se and 2 planes of Cd at the surface, which corresponds to 0.4 mmol. The particles are suspended in 10 mL, so the concentration of surface Cd is 0.04 mmol/mL.

*Synthesis of small 4 ML CdSe NPLs :* In a three-neck flask, 170 mg of $Cd(Myr)_2$, 12 mg of Se and 15mL of ODE are degassed at 50°C for 30 min. Under Argon, the mixture is heated up to 240°C. At 220°C, when the solution is a bright orange, 53 mg of $Cd(Ac)_2.2H_2O$ is swiftly introduced, and the reaction is left 10min. During the cooling, 1mL OA is added to the flask. The particles are washed and suspended in 10mL of hexane for further use. For 4 ML CdSe NPLs, the synthesis process conducts to a mix of NPLs and spherical QDs. A good approximation is that 50% of the Se ends in NPLs and 50% in the QDs. Thus, there are 0.075 mmol of Se in NPLs, so 0.038 mmol of surface Cd and the final concentration in a small 4MLs CdSe NPLs synthesis is 0.0038 mmol/mL.

*Lateral growth of 4 ML CdSe NPLs :* 1 mL of the small 4MLs CdSe NPLs cores solution is precipitated and suspended in 3 mL ODE. In a three-neck flask, the mixture is degassed with 150µL OA at 50°C for 45 min, after which the atmosphere is switched to Argon, and the temperature is set to 240°C. At around 180°C, 100 mg $Cd(Ac)_2.2H_2O$ is introduced into the flask. After reaching 240°C, a growth solution made of 200 µL of TOP-Se 1M in 1.8 mL ODE is injected at a rate of 1 mL/h for 20 min and at 2 mL/h for the remaining growth solution. The solution is cooled down to room temperature and the particles are washed twice, before being suspended in 4 mL hexane. *Alternatively,* 1 mL of the small 4MLs CdSe NPLs cores solution is precipitated and suspended in 3 mL ODE. In a three-neck flask, the mixture is degassed with 266 mg of Cd(Ac)2.2H2O at 60°C for 1h, after which the atmosphere is switched to Ar, and the temperature is set to 240°C. At around 190°C, 300 µL of OA are introduced into the flask, and at 210°C, 5 mL of Se-ODE 0.1 M is injected at 5 mL/h. After full injection of the growth solution, the mixture is kept at 240°C for 1 more hour. The solution is then cooled down to room temperature and the particles are washed twice, before being suspended in 10 mL hexane.

*Synthesis of 5 ML and 6 ML CdSe NPLs:* These NPLs are synthesized from respectively 3 ML and extended 4 ML NPLs by the colloidal atomic layer deposition (c-ALD). In a Falcon of 15 mL, 2 mL of the as made CdSe NPLs is diluted with 2 mL of hexane, and 20 µL of TBP and 20 µL of ethanol are added into the Falcon. 40 mg of $NaBH_4$ (1.1mmol) is dissolved in 1mL of the mixture 1:1 of NMF and ethanol, and 24 mg of Se powder (0.3mmol) is added into the $NaBH_4$ solution. 500 µL of the Se precursor is added into the NPLs solution as soon as the $NaBH_4$–Se solution becomes colorless. The solution is vortexed for 2min, and a phase separation is observed. 1 mL of NMF is added to the mixture to dissolve again the NPLs. The colorless supernatant phase which contains hexane is removed; this step is repeated after adding 2 mL of hexane, 20 µL of TBP and20 µL of ethanol in order to wash the Se in excess and to avoid the formation of polyselenides. Then the colored phase is centrifuged with 2 mL of toluene and redispersed in 3 mL of NMF. 2 mL of $Cd(Ac)_2$ 0.1 M (50 mg of $Cd(Ac)_2$ in 2 mL of NMF, 0.2 mmol) is added to the NPLs solution, and the mixture is vortexed for 2 min. 2 mL of hexane and 200 µL of methanol, 1mL of OA are added into the mixture to facilitate the phase separation. Then, the colored supernatant phase is centrifuged twice with 5 mL of hexane and 5 mL of ethanol. The NPLs are redispersed in 6 mL of ODE and are transferred into a 25 mL three-neck flask containing 50 mg of $Cd(Ac)_2$ (0.2 mmol), 70 µL of TBP, and 70 µL of OA (0.22 mmol). The mixture is degassed at room temperature for 30 min and then heated to 230°C for 20 min under Argon. The final NPLs are cooled down to room temperature and centrifuged twice with 10 mL of hexane and 10mL of ethanol and suspended in 10 mL hexane. The concentration of surface Cd is diluted by 5 compared to 3 and 4 ML core NPLs.

*General purification protocol for CdSe NPLs :* The reaction products are mixed with 15 mL ethanol and 15 mL hexane by sonication. The suspension is centrifuged for 5 min at 6,000 RPM, and the supernatant is discarded whereas the precipitate is resuspended in hexane.

<u>Surface ligand exchange</u>

Ligand exchange to chiral dicarboxylates: A 0.1 M solution of TA in ethanol is prepared by sonication and strong stirring of 2 mmol of the L-TA, D-TA or R-TA in 20 mL ethanol until complete dissolution. In a vial, 500 µL of the previous solution is added to 100 µL of TOP under stirring. The NPLs are added with a volume containing 0.001 mmol of surface cadmium in order to get a ratio of 50 ligands per surface cadmium. The exchange is performed at room temperature. At the end of the exchange, the

particles are washed by precipitation with the addition of a few drops of hexane, for 5 min at 12,000 RPM, and resuspended in ethanol for characterization.

Characterization techniques

Absorption spectroscopy: Absorption spectra are recorded at room temperature on an Agilent Cary 5000 UV-Vis-NIR spectrophotometer. During measurements, small fractions of particles are taken out from initial colloidal solutions and diluted in hexane or ethanol in a quartz cuvette.

CD spectroscopy: CD and absorption spectra are recorded at room temperature on a Jasco J-815 spectrometer equipped with a 150W air-cooled Xe lamp. Measurements are acquired from 800 nm to 300 nm with a step size of 1 nm and a bandwidth of 1 nm, at a scanning speed of 200 nm/min. The chiral nanoparticles are diluted in ethanol and placed in a HELMA QS 100-10-40 quartz cuvette.

LD spectroscopy: LD, along with CD and absorption spectra on a Jasco J-1500. The same acquisition procedure is used with respect to CD spectroscopy on the Jasco J-815.

TEM analysis: TEM images are recorded on a JEOL 2010 transmission electron microscope at a working voltage of 200 kV. The nanocrystals are drop-casted onto a copper grid covered with amorphous carbon film, and the grid is degassed a few hours under vacuum.

Capillary XRD analysis : XRD signals are recorded in a capillary on a Rigaku MicroMax 007HF diffractometer with a Mo-K$\alpha$ radiation. Experimental conditions of 50kV in voltage and 24mA in current are set. Diffraction patterns are obtained this time around, under the capillary mode where the nanoparticles are suspended in hexane or ethanol as the organic solvent. Signal acquisitions are done in the $2\theta$ range between (0.03-64.9)° with a step size of 0.030°.

FTIR spectroscopy : Fourier transform infrared spectroscopy spectra are recorded on a Bruker Vertex 70 spectrometer at room temperature, in the wavenumber range between 400 and 4000 $cm^{-1}$. During measurements, concentrated nanoparticle colloidal solutions are drop-cast onto the detection zone, and signals are acquired after solvent evaporation.

EDX spectroscopy analysis : A few drops of a highly concentrated solution of NPLs is drop-casted onto a (100)-cut Si wafer. EDX spectra are recorded on a FEI Magellan scanning electron microscope operated at 20 kV and 1.6 nA, equipped with an Oxford probe.

DFT simulations :

*Ab initio* method was applied on 4 ML CdSe with ligands in two configurations using VASP package.[69,70] The unit cell consists of 184 atoms and a 1.5-nm vacuum to separate slabs in the periodic boundary condition. For the large size of the unit cell ($1.21 \times 1.21 \times 3.5\ nm^3$), computation only considers the Gamma point in the Brillouin zone. The cut-off energy of the plane-wave basis is set at 400 eV, and convergence of total energy is set at $10^{-8}$ eV for the electronic step. The positions of atoms were optimized using density functional theory with PBE functional,[71] and the total energy is converged within $10^{-5}$ eV for the Ionic step.

**Associated content**

The supporting information is available free of charge at…

Supporting information include the optimization of ligand exchange on 4 ML CdSe NPLs, the effect of TOP along the ligand exchange, the effect of surface chemistry on the ligand exchange kinetic, The characterization of NPLs after ligand exchange, the effect of temperature on the kinetic of the ligand exchange, the binding characterization of tartrate ligands by DFT, the simulations of diffraction patterns, the characterization of stress in NPLs with various ligands, the optical characterization of various NPLs capped with tartrate ligands and the characterization of linear dichroism linear birefringence in NPLs

**Acknowledgments**

We thank Avinabh Choudhary for samples preparations. We thank Matthieu Raynal for giving us access to a JASCO 1500 for LD measurements. This project has received funding from the European Research Council (ERC) under the European Union's Horizon 2020 research and innovation program (Ne2DeM grant agreement n° 853049)

**References**

(1) Diroll, B. T.; Guzelturk, B.; Po, H.; Dabard, C.; Fu, N.; Makke, L.; Lhuillier, E.; Ithurria, S. 2D II-VI Semiconductor Nanoplatelets: From Material Synthesis to Optoelectronic Integration. *Chem. Rev.* **2023**, *123* (7), 3543–3624.

(2) Izquierdo, E.; Robin, A.; Keuleyan, S.; Lequeux, N.; Lhuillier, E.; Ithurria, S. Strongly Confined HgTe 2D Nanoplatelets as Narrow near Infrared Emitters. *J. Am. Chem. Soc.* **2016**, *138* (33), 10496–10501.

(3) Yoon, D. E.; Kim, W. D.; Kim, D.; Lee, D.; Koh, S.; Bae, W. K.; Lee, D. C. Origin of Shape-Dependent Fluorescence Polarization from CdSe Nanoplatelets. *J. Phys. Chem. C* **2017**, *121* (39), 24837–24844.

(4) Achtstein, A. W.; Antanovich, A.; Prudnikau, A.; Scott, R.; Woggon, U.; Artemyev, M. Linear Absorption in CdSe Nanoplates: Thickness and Lateral Size Dependency of the Intrinsic Absorption. *J. Phys. Chem. C* **2015**, *119* (34), 20156–20161.

(5) Hao, J.; Zhao, F.; Wang, Q.; Lin, J.; Chen, P.; Li, J.; Zhang, D.; Chen, M.; Liu, P.; Delville, M. H.; He, T.; Cheng, J.; Li, Y. Optically Active CdSe/CdS Nanoplatelets Exhibiting Both Circular Dichroism and Circularly Polarized Luminescence. *Adv. Opt. Mater.* **2021**, *2101142*, 1–10.

(6) Kotov, N. A.; Liz-Marzán, L. M.; Wang, Q. Chiral Nanomaterials: Evolving Rapidly from Concepts to Applications. *Mater. Adv.* **2022**, 3677–3679.

(7) Ma, W.; Xu, L.; Wang, L.; Xu, C.; Kuang, H. Chirality-Based Biosensors. *Adv. Sci. News* **2019**, *29*, 1805512.

(8) Wang, F.; Yue, X.; Ding, Q.; Lin, H.; Xu, C.; Li, S. Chiral Inorganic Nanomaterials for Biological Applications. *Nanoscale* **2023**, *15* (6), 2541–2552.

(9) Zhan, X.; Xu, F. F.; Zhou, Z.; Yan, Y.; Yao, J.; Zhao, Y. S. 3D Laser Displays Based on Circularly Polarized Lasing from Cholesteric Liquid Crystal Arrays. *Adv. Mater.* **2021**, *33* (37), 1–7.

(10) Mondal, P. C.; Asthana, D.; Parashar, R. K.; Jadhav, S. Imprinting Chirality in Inorganic Nanomaterials for Optoelectronic and Bio-Applications: Strategies, Challenges, and

Opportunities. *Mater. Adv.* **2021**, *2* (23), 7620–7637.

(11) Rukhlenko, I. D.; Baimuratov, A. S.; Tepliakov, N. V.; Baranov, A. V.; Fedorov, A. V. Shape-Induced Optical Activity of Chiral Nanocrystals. *Opt. Lett.* **2016**, *41* (11), 2438.

(12) Wang, P. P.; Yu, S. J.; Ouyang, M. Assembled Suprastructures of Inorganic Chiral Nanocrystals and Hierarchical Chirality. *J. Am. Chem. Soc.* **2017**, *139* (17), 6070–6073.

(13) Feng, W.; Kim, J. Y.; Wang, X.; Calcaterra, H. a.; Qu, Z.; Meshi, L.; Kotov, N. a. Assembly of Mesoscale Helices with Near-Unity Enantiomeric Excess and Light-Matter Interactions for Chiral Semiconductors. *Sci. Adv.* **2017**, *3* (3), 1–13.

(14) Kuznetsova, V.; Gromova, Y.; Martinez-Carmona, M.; Purcell-Milton, F.; Ushakova, E.; Cherevkov, S.; Maslov, V.; Gun'Ko, Y. K. Ligand-Induced Chirality and Optical Activity in Semiconductor Nanocrystals: Theory and Applications. *Nanophotonics* **2020**, *10* (2), 797–824.

(15) Lu, J.; Wu, W.; Colombari, F. M.; Jawaid, A.; Seymour, B.; Whisnant, K.; Zhong, X.; Choi, W.; Lahann, J.; Vaia, R. A.; de Moura, A. F.; Nepal, D.; Kotov, N. A. Nano-Achiral Complex Composites for Extreme Polarization Optics. *Nature* **2024**, *630* (8018), 860–865.

(16) Yeom, J.; Yeom, B.; Chan, H.; Smith, K. W.; Dominguez-Medina, S.; Bahng, J. H.; Zhao, G.; Chang, W. S.; Chang, S. J.; Chuvilin, A.; Melnikau, D.; Rogach, A. L.; Zhang, P.; Link, S.; Král, P.; Kotov, N. a. Chiral Templating of Self-Assembling Nanostructures by Circularly Polarized Light. *Nat. Mater.* **2015**, *14* (1), 66–72.

(17) Lee, H. E.; Ahn, H. Y.; Mun, J.; Lee, Y. Y.; Kim, M.; Cho, N. H.; Chang, K.; Kim, W. S.; Rho, J.; Nam, K. T. Amino-Acid- A Nd Peptide-Directed Synthesis of Chiral Plasmonic Gold Nanoparticles. *Nature* **2018**, *556* (7701), 360–364.

(18) Tepliakov, N. V.; Baimuratov, A. S.; Vovk, I. a.; Leonov, M. Y.; Baranov, A. V.; Fedorov, A. V.; Rukhlenko, I. D. Chiral Optical Properties of Tapered Semiconductor Nanoscrolls. *ACS Nano* **2017**, *11* (7), 7508–7515.

(19) Guillemeney, L.; Lermusiaux, L.; Landaburu, G.; Wagnon, B.; Abécassis, B. Curvature and Self-Assembly of Semi-Conducting Nanoplatelets. *Commun. Chem.* **2022**, *5* (1), 1–11.

(20) Bouet, C.; Mahler, B.; Nadal, B.; Abecassis, B.; Tessier, M. D.; Ithurria, S.; Xu, X.; Dubertret, B. Two-Dimensional Growth of CdSe Nanocrystals, from Nanoplatelets to Nanosheets. *Chem. Mater.* **2013**, *25* (4), 639–645.

(21) Ithurria, S.; Dubertret, B. Quasi 2D Colloidal CdSe Platelets with Thicknesses Controlled at the Atomic Level. *J. Am. Chem. Soc.* **2008**, *130* (49), 16504–16505.

(22) Liu, Y. H.; Wayman, V. L.; Gibbons, P. C.; Loomis, R. a.; Buhro, W. E. Origin of High Photoluminescence Efficiencies in CdSe Quantum Belts. *Nano Lett.* **2010**, *10* (1), 352–357.

(23) Joo, J.; Son, J. S.; Kwon, S. G.; Yu, J. H.; Hyeon, T. Low-Temperature Solution-Phase Synthesis of Quantum Well Structured CdSe Nanoribbons. *J. Am. Chem. Soc.* **2006**, *128* (17), 5632–5633.

(24) Dufour, M.; Qu, J.; Greboval, C.; Méthivier, C.; Ithurria, S. Halide Ligands to Release Strain in Cadmium Chalcogenide Nanoplatelets and Achieve High Brightness. *ACS Nano* **2019**, *13* (5), 5326–5334.

(25) Antanovich, A.; Achtstein, A. W.; Matsukovich, A.; Prudnikau, A.; Bhaskar, P.; Gurin, V.; Molinari, M.; Artemyev, M. A Strain-Induced Exciton Transition Energy Shift in CdSe

Nanoplatelets: The Impact of an Organic Ligand Shell. *Nanoscale* **2017**, *9* (45), 18042–18053.

(26) Armon, S.; Efrati, E.; Kupferman, R.; Sharon, E. Geometry and Mechanics in the Opening of Chiral Seed Pods. *Science* **2011**, *333*, 1726.

(27) Monego, D.; Dutta, S.; Grossman, D.; Krapez, M.; Bauer, P.; Hubley, A.; Margueritat, J.; Mahler, B.; Widmer-Cooper, A.; Abécassis, B. Ligand-Induced Incompatible Curvatures Control Ultrathin Nanoplatelet Polymorphism and Chirality. *Proc. Natl. Acad. Sci.* **2024**, *121* (9), 1–8.

(28) Baimuratov, A. S.; Pereziabova, T. P.; Zhu, W.; Leonov, M. Y.; Baranov, A. V.; Fedorov, A. V.; Rukhlenko, I. D. Optical Anisotropy of Topologically Distorted Semiconductor Nanocrystals. *Nano Lett.* **2017**, *17* (9), 5514–5520.

(29) Baimuratov, A. S.; Gun'ko, Y. K.; Shalkovskiy, A. G.; Baranov, A. V.; Fedorov, A. V.; Rukhlenko, I. D. Optical Activity of Chiral Nanoscrolls. *Adv. Opt. Mater.* **2017**, *5* (16), 1–6.

(30) Po, H.; Dabard, C.; Roman, B.; Reyssat, E.; Bico, J.; Baptiste, B.; Lhuillier, E.; Ithurria, S. Chiral Helices Formation by Self-Assembled Molecules on Semiconductor Flexible Substrates. *ACS Nano* **2022**, *16*, 2901–2909.

(31) Liu, P.; Battie, Y.; Decossas, M.; Tan, S.; Pouget, E.; Okazaki, Y.; Sagawa, T.; Oda, R. Chirality Induction to CdSe Nanocrystals Self-Organized on Silica Nanohelices: Tuning Chiroptical Properties. *ACS Nano* **2021**, *15* (10), 16411–16421.

(32) Jana, S.; De Frutos, M.; Davidson, P.; Abécassis, B. Ligand-Induced Twisting of Nanoplatelets and Their Self-Assembly into Chiral Ribbons. *Sci. Adv.* **2017**, *3* (9), e1701483.

(33) Gao, X.; Yang, X.; Lv, J.; Zhao, L.; Sui, X.; Zhang, X.; Xie, Y.; Tang, Z. Induced Huge Optical Activity in Nanoplatelet Superlattice. *J. Am. Chem. Soc.* **2024**, 4–11.

(34) Yao, Y.; Ugras, T. J.; Meyer, T.; Dykes, M.; Wang, D.; Arbe, A.; Bals, S.; Kahr, B.; Robinson, R. D. Extracting Pure Circular Dichroism from Hierarchically Structured CdS Magic Cluster Films. *ACS Nano* **2022**, *16* (12), 20457–20469.

(35) Zhang, Z.; Wang, Z.; Sung, H. H. Y.; Williams, I. D.; Yu, Z. G.; Lu, H. Revealing the Intrinsic Chiroptical Activity in Chiral Metal-Halide Semiconductors. *J. Am. Chem. Soc.* **2022**, *144* (48), 22242–22250.

(36) Tohgha, U.; Deol, K. K.; Porter, A. G.; Bartko, S. G.; Choi, J. K.; Leonard, B. M.; Varga, K.; Kubelka, J.; Muller, G.; Balaz, M. Ligand Induced Circular Dichroism and Circularly Polarized Luminescence in Cdse Quantum Dots. *ACS Nano* **2013**, *7* (12), 11094–11102.

(37) Tohgha, U.; Varga, K.; Balaz, M. Achiral CdSe Quantum Dots Exhibit Optical Activity in the Visible Region upon Post-Synthetic Ligand Exchange with D- or L-Cysteine. *Chem. Commun.* **2013**, *49* (18), 1844–1846.

(38) Puri, M.; Ferry, V. E. Circular Dichroism of CdSe Nanocrystals Bound by Chiral Carboxylic Acids. *ACS Nano* **2017**, *11* (12), 12240–12246.

(39) Kurtina, D. A.; Zaytsev, V. B.; Vasiliev, R. B. Chirality in Atomically Thin CdSe Nanoplatelets Capped with Thiol-Free Amino Acid Ligands: Circular Dichroism vs. Carboxylate Group Coordination. *Materials* **2024**, *17* (1), 237.

(40) Curti, L.; Landaburu, G.; Abécassis, B.; Fleury, B. Chiroptical Properties of Semiconducting Nanoplatelets Functionalized by Tartrate Derivatives. *Langmuir* **2024**, *40* (22), 11481–11490.

(41) Kurtina, D. A.; Garshev, A. V.; Vasil'Eva, I. S.; Shubin, V. V.; Gaskov, A. M.; Vasiliev, R. B. Atomically Thin Population of Colloidal CdSe Nanoplatelets: Growth of Rolled-up Nanosheets and Strong Circular Dichroism Induced by Ligand Exchange. *Chem. Mater.* **2019**, *31* (23), 9652–9663.

(42) Lu, H.; Xiao, C.; Song, R.; Li, T.; Maughan, A. E.; Levin, A.; Brunecky, R.; Berry, J. J.; Mitzi, D. B.; Blum, V.; Beard, M. C. Highly Distorted Chiral Two-Dimensional Tin Iodide Perovskites for Spin Polarized Charge Transport. *J. Am. Chem. Soc.* **2020**, *142* (30), 13030–13040.

(43) Elliott, S. D.; Moloney, M. P.; Gun'ko, Y. K. Chiral Shells and Achiral Cores in CdS Quantum Dots. *Nano Lett.* **2008**, *8* (8), 2452–2457.

(44) Zhou, Y.; Yang, M.; Sun, K.; Tang, Z.; Kotov, N. A. Similar Topological Origin of Chiral Centers in Organic and Nanoscale Inorganic Structures: Effect of Stabilizer Chirality on Optical Isomerism and Growth of Cdte Nanocrystals. *J. Am. Chem. Soc.* **2010**, *132* (17), 6006–6013.

(45) Zhao, J.; Wang, Y.; Wang, T.; Wang, Y. Chiral Defect-Induced Blue Photoluminescence and Circularly Polarized Luminescence of Zero-Dimensional Cs4PbBr6 Perovskite Nanocrystals. *Inorg. Chem. Front.* **2024**, *11*, 4424.

(46) Mukhina, M. V.; Maslov, V. G.; Baranov, A. V.; Fedorov, A. V.; Orlova, A. O.; Purcell-Milton, F.; Govan, J.; Gun'Ko, Y. K. Intrinsic Chirality of CdSe/ZnS Quantum Dots and Quantum Rods. *Nano Lett.* **2015**, *15* (5), 2844–2851.

(47) Ma, S.; Jung, Y. K.; Ahn, J.; Kyhm, J.; Tan, J.; Lee, H.; Jang, G.; Lee, C. U.; Walsh, A.; Moon, J. Elucidating the Origin of Chiroptical Activity in Chiral 2D Perovskites through Nano-Confined Growth. *Nat. Commun.* **2022**, *13* (1), 1–10.

(48) Ben-Moshe, A.; Teitelboim, A.; Oron, D.; Markovich, G. Probing the Interaction of Quantum Dots with Chiral Capping Molecules Using Circular Dichroism Spectroscopy. *Nano Lett.* **2016**, *16* (12), 7467–7473.

(49) Cheng, J.; Hao, J.; Liu, H.; Li, J.; Li, J.; Zhu, X.; Lin, X.; Wang, K.; He, T. Optically Active CdSe-Dot/CdS-Rod Nanocrystals with Induced Chirality and Circularly Polarized Luminescence. *ACS Nano* **2018**, *12* (6), 5341–5350.

(50) Gao, X.; Zhang, X.; Zhao, L.; Huang, P.; Han, B.; Lv, J.; Qiu, X.; Wei, S. H.; Tang, Z. Distinct Excitonic Circular Dichroism between Wurtzite and Zincblende CdSe Nanoplatelets. *Nano Lett.* **2018**, *18* (11), 6665–6671.

(51) Yang, G.; Kazes, M.; Oron, D. Chiral 2D Colloidal Semiconductor Quantum Wells. *Adv. Funct. Mater.* **2018**, *28*, 1802012.

(52) Kurtina, D. A.; Grafova, V. P.; Vasil'eva, I. S.; Maksimov, S. V.; Zaytsev, V. B.; Vasiliev, R. B. Induction of Chirality in Atomically Thin ZnSe and CdSe Nanoplatelets: Strengthening of Circular Dichroism via Different Coordination of Cysteine-Based Ligands on an Ultimate Thin Semiconductor Core. *Materials* **2023**, *16* (3), 1073.

(53) Cui, Y.; Jiang, J.; Mi, W.; Xiao, Y. Synthesis of Five-Layered Chiral Perovskite Nanowires and Enacting Chiroptical Activity Regulation. *Cell Reports Phys. Sci.* **2023**, *4* (3), 101299.

(54) Walters, R. S.; Kraml, C. M.; Byrne, N.; Ho, D. M.; Qin, Q.; Coughlin, F. J.; Bernhard, S.; Pascal, R. A. Configurationally Stable Longitudinally Twisted Polycyclic Aromatic Compounds. *J. Am. Chem. Soc.* **2008**, *130* (48), 16435–16441.

(55) Li, J. K.; Chen, X. Y.; Guo, Y. L.; Wang, X. C.; Sue, A. C. H.; Cao, X. Y.; Wang, X. Y. B,N-Embedded Double Hetero[7]Helicenes with Strong Chiroptical Responses in the Visible Light Region. *J. Am. Chem. Soc.* **2021**, *143* (43), 17958–17963.

(56) Guerrero-Martínez, A.; Auguié, B.; Alonso-Gómez, J. L.; Džolić, Z.; Gómez-Graña, S.; Žinić, M.; Cid, M. M.; Liz-Marzán, L. M. Intense Optical Activity from Three-Dimensional Chiral Ordering of Plasmonic Nanoantennas. *Angew. Chemie Int. Ed.* **2011**, *50* (24), 5499–5503.

(57) Cai, J.; Liu, A. A.; Shi, X. H.; Fu, H.; Zhao, W.; Xu, L.; Kuang, H.; Xu, C.; Pang, D. W. Enhancing Circularly Polarized Luminescence in Quantum Dots through Chiral Coordination-Mediated Growth at the Liquid/Liquid Interface. *J. Am. Chem. Soc.* **2023**, *145* (44), 24375–24385.

(58) Fecher, G. H.; Kübler, J.; Felser, C. Chirality in the Solid State: Chiral Crystal Structures in Chiral and Achiral Space Groups. *Materials* **2022**, *15* (17), 1–32.

(59) Homberg, A.; Brun, E.; Zinna, F.; Pascal, S.; Górecki, M.; Monnier, L.; Besnard, C.; Pescitelli, G.; Di Bari, L.; Lacour, J. Combined Reversible Switching of ECD and Quenching of CPL with Chiral Fluorescent Macrocycles. *Chem. Sci.* **2018**, *9* (35), 7043–7052.

(60) Zhang, J.; Zhang, H.; Cao, W.; Pang, Z.; Li, J.; Shu, Y.; Zhu, C.; Kong, X.; Wang, L.; Peng, X. Identification of Facet-Dependent Coordination Structures of Carboxylate Ligands on CdSe Nanocrystals. *J. Am. Chem. Soc.* **2019**, *141* (39), 15675–15683.

(61) Owen, J. The Coordination Chemistry of Nanocrystal Surfaces. *Science (80-. ).* **2015**, *347* (6222), 615–616.

(62) Anderson, N. C.; Hendricks, M. P.; Choi, J. J.; Owen, J. S. Ligand Exchange and the Stoichiometry of Metal Chalcogenide Nanocrystals: Spectroscopic Observation of Facile Metal-Carboxylate Displacement and Binding. *J. Am. Chem. Soc.* **2013**, *135* (49), 18536–18548.

(63) Deacon, G. B.; Phillips, R. J. RELATIONSHIPS BETWEEN THE CARBON-OXYGEN STRETCHING FREQUENCIES OF CARBOXYLATO COMPLEXES AND THE TYPE OF CARBOXYLATE COORDINATION. *Coord. Chem. Rev.* **1980**, *33*, 227–250.

(64) Heckmann, J.; Scott, R.; Prudnikau, A. V.; Antanovich, A.; Owschimikow, N.; Artemyev, M.; Climente, J. I.; Woggon, U.; Grosse, N. B.; Achtstein, A. W. Directed Two-Photon Absorption in CdSe Nanoplatelets Revealed by k-Space Spectroscopy. *Nano Lett.* **2017**, *17* (10), 6321–6329.

(65) O'Reilly, E. P. Valence Band Engineering in Strained-Layer Structures. *Semicond. Sci. Technol.* **1989**, *4* (3), 121–137.

(66) Martinet, Q.; Baronnier, J.; Girard, A.; Albaret, T.; Saviot, L.; Mermet, A.; Abecassis, B.; Margueritat, J.; Mahler, B. Ligand-Dependent Nano-Mechanical Properties of CdSe Nanoplatelets: Calibrating Nanobalances for Ligand Affinity Monitoring. *Nanoscale* **2021**, *13* (18), 8639–8647.

(67) Diroll, B. T. Ligand-Dependent Tuning of Interband and Intersubband Transitions of Colloidal CdSe Nanoplatelets. *Chem. Mater.* **2020**, *32* (13), 5916–5923.

(68) Greenwood, A. R.; Mazzotti, S.; Norris, D. J.; Galli, G. Determining the Structure–Property Relationships of Quasi-Two-Dimensional Semiconductor Nanoplatelets. *J. Phys. Chem. C* **2021**, *125* (8), 4820–4827.

(69) Kresse, G.; Furthmüller, J. Efficient Iterative Schemes for Ab Initio Total-Energy Calculations Using a Plane-Wave Basis Set. *Phys. Rev. B* **1996**, *54* (16), 11169–11186.

(70) Kresse, G.; Furthmüller, J. Efficiency of Ab-Initio Total Energy Calculations for Metals and Semiconductors Using a Plane-Wave Basis Set. *Comput. Mater. Sci.* **1996**, *6* (1), 15–50.

(71) Perdew, J. P.; Burke, K.; Ernzerhof, M. Generalized Gradient Approximation Made Simple. *Phys. Rev. Lett.* **1996**, *77* (18), 3865–3868.

Table of Content